Chinese Chemical Letters 36 (2025) 110016

Contents lists available at ScienceDirect

Chinese Chemical Letters

journal homepage: www.elsevier.com/locate/cclet

Bimetallic zeolitic imidazolate framework derived hollow layered double hydroxide with tailorable interlayer spacing for nickel-zinc batteries

Hui Yang, Guangxun Zhang, Yueyao Sun, Huijie Zhou, Huan Pang*

School of Chemistry and Chemical Engineering, Yangzhou University, Yangzhou 225009, China

ARTICLE INFO

Article history:
Received 18 March 2024
Revised 18 April 2024
Accepted 14 May 2024
Available online 16 May 2024

Keywords:
Nickel-zinc battery
Hollow
Interlayer spacing
Layered double hydroxide
Zeolitic imidazolate framework

ABSTRACT

Rationally design the morphology and structure of electroactive nanomaterials is an effective approach to enhance the performance of aqueous batteries. Herein, we co-engineered the hollow architecture and interlayer spacing of layered double hydroxides (LDH) to achieve high electrochemical activity. The hierarchical hollow LDH was prepared from bimetallic zeolitic imidazolate frameworks (ZIF) by a facile cation exchange strategy. Zn and Cu elements were selected as the second metals incorporated in Co-ZIF. The characteristics of the corresponding derivatives were studied. Besides, the transformation mechanism of CoZn-ZIF into nanosheet-assembled hollow CoZnNi LDH (denoted as CoZnNi-OH) was systematically investigated. Importantly, the interlayer spacing of CoZnNi-OH expands due to Zn^{2+} incorporation. The prepared CoZnNi-OH offers large surface area, exposed active sites, and rapid mass transfer/diffusion rate, which lead to a significant enhancement in the specific capacitance, rate performance, and cycle stability of CoZnNi-OH electrode. In addition, the aqueous alkaline CoZnNi-OH//Zn showed a maximum energy density/power density of 0.924 mWh/cm^2, 8.479 mW/cm^2. This work not only raises an insightful strategy for regulating the morphology and interlayer spacing of LDH, but also provides a reference of designing hollow nickel-based nanomaterials for aqueous batteries.

Hollow architectures refer to well-defined interior cavities and boundaries. Such unique morphology exhibits many advantages, including large enclosed cavities, large specific surface area, and sturdy structure [1–4]. Therefore, designing fundamental materials with hollow structures is a subject of great interest to researchers. These hollow nanomaterials have shown broad application prospects in batteries, supercapacitors, electrocatalysis, drug delivery, gas sensors, photocatalysis, environmental treatment, and life sciences [5–9]. However, obtaining well-defined hollow architectures in a green and efficient procedure remains a challenging project.

Metal-organic frameworks (MOFs) are a common class of porous crystalline materials consisting of organic ligands and inorganic nodes [10–12]. Among various MOFs, zeolitic imidazolate framework (ZIF) is a typical subclass. Due to their diverse geometric shapes and simple preparation, ZIFs become popular precursors for derivatives [13]. Generally, ZIF-derived nanomaterials have outstanding mechanical and chemical stabilities, high conductivity, various functionalities, and large specific surface areas [14,15]. Among various derivatives, ZIF-derived layered double hydroxide (LDH), as one of important energy-related materials, has been noticed on account of their adjustable morphology, controllable composition, and excellent redox activity [16,17]. However, most ZIF-derived LDHs are synthesized from monometallic ZIF precursors, and few bimetallic ZIF-derived LDH have been reported. Therefore, it is of great significance to explore the reaction mechanism and composition changes in the synthesis process of bimetallic ZIF-derived LDH. Besides, modulating the interlayer spacing of LDH is of great significance for improving the electrochemical properties of LDH, since the larger interlayer spacing can facilitate ion diffusion during electrochemical reaction.

Recently, aqueous batteries have attracted much attention from researchers because of their cost and security advantages [18]. In particular, the aqueous nickel-zinc battery has the advantages of large energy density, rich metal resource, and environmentally friendly [19,20]. However, the development of the battery is still restricted by the capacity and stability of nickel-based cathode. Thus, it is necessary to explore the advanced nickel-based cathode. To date, many strategies have been proposed to enhance the stability and electrochemical dynamics of nickel-based nanomateri-

* Corresponding author.
E-mail address: panghuan@yzu.edu.cn (H. Pang).

https://doi.org/10.1016/j.cclet.2024.110016
1001-8417/

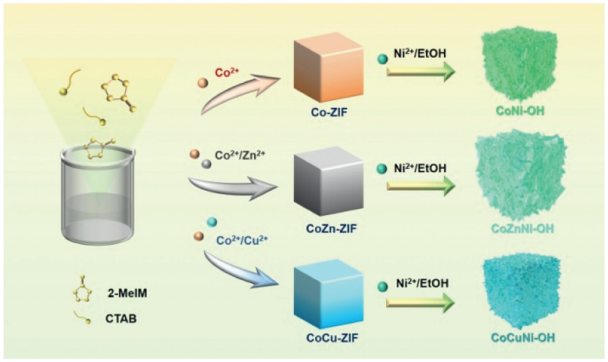

Fig. 1. Schematic diagram of the preparation of ZIF nanocubes and LDH nanoboxes.

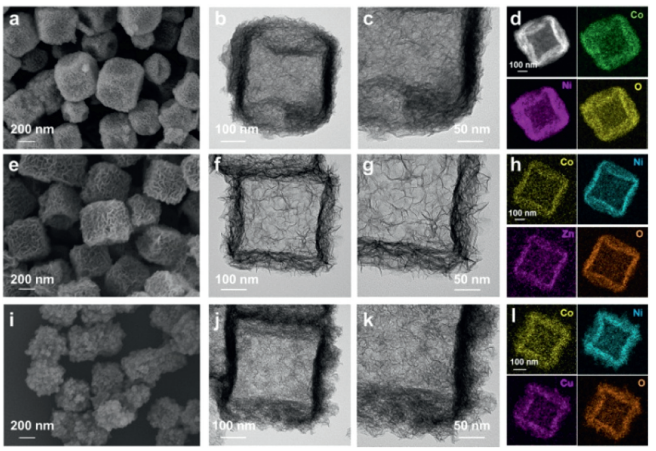

Fig. 2. (a) SEM image, (b, c) TEM images, (d) HAADF-STEM image and corresponding elemental mapping of CoNi-OH. (e) SEM image, (f, g) TEM images, (h) elemental mapping of CoZnNi-OH. (i) SEM image, (j, k) TEM images, (l) elemental mapping of CoCuNi-OH.

als, such as nanostructure construction and composition optimization [21,22]. MOF-derived LDH with adjustable composition, hierarchical nanostructure, and considerable redox activity is a promising cathode nanomaterial for achieving high performance aqueous nickel-zinc battery.

Herein, we designed bimetallic ZIF-derived LDH with hierarchical hollow structure and adjustable interlayer spacing by a facile cation exchange strategy. Zn and Cu elements were selected as the second metals incorporated in Co-ZIF. The characteristics of the corresponding derivatives were studied. Besides, the transformation mechanism of CoZn-ZIF into CoZnNi-OH was systematically investigated. Notably, the hollow architecture and expanded interlayer spacing of CoZnNi-OH not only provides a large electrolyte contact area, but also reduces volume expansion during electrochemical reactions. Especially for the aqueous alkaline CoZnNi-OH//Zn battery, the maximum energy density/power density reached 0.924 mWh/cm^2, 8.479 mW/cm^2. This work is a valuable reference of co-engineering the hollow architecture and interlayer spacing of LDH.

The synthesis procedure of ZIF nanocubes and LDH nanoboxes is shown in Fig. 1. ZIF nanocubes with different metal centers were synthesized in an aqueous solution through co-precipitation method. The morphology of ZIFs was observed *via* scanning and transmission electron microscopy (SEM/TEM) (Fig. S1 in Supporting information). Co-ZIF, CoZn-ZIF, and CoCu-ZIF exhibit regular hexahedral morphology, with sizes ranging from 450 nm to 550 nm. Figs. S2 and S3 (Supporting information) show the similar XRD diffraction peaks and FTIR transmission peaks of Co-ZIF, CoZn-ZIF, and CoCu-ZIF, demonstrating the similar crystal structure and functional groups of the synthesized ZIF precursors. Besides, the energy dispersive spectrometer (EDS) implies the existence of Cu and Zn element in ZIFs (Fig. S4 in Supporting information).

To obtain hollow LDHs, a green and convenient cation exchange strategy was adopted. Using ZIFs as the self-sacrificial templates, Ni^{2+} as the cationic etchant, and ethanol as the reaction solvent, LDHs were synthesized under room temperature. The LDH nanoboxes transformed from Co-ZIF, CoZn-ZIF, and CoCu-ZIF were named CoNi-OH, CoCuNi-OH, and CoZnNi-OH, respectively. The morphology of CoNi-OH, CoCuNi-OH, and CoZnNi-OH can be observed in Figs. 2a-c, Figs. 2e-g, and Figs. 2i-k, respectively. All the samples exhibit hollow structures that were assembled by ultrathin nanosheets. Notably, the nanosheets in the hollow assembly show differences. Compared with the nanosheet size of CoNi-OH sample, CoCuNi-OH is smaller, while CoZnNi-OH is larger. This could be attributed to the different coordination bond strength between the metal center and di-methylimidazole in the crystal structure of ZIFs. The coordination bond in CoZn-ZIF is more stable than that of CoCu-ZIF, so the bond breaking speed of CoZn-ZIF is slower than that of CoCu-ZIF, and the forming speed of CoZnNi-OH is also slower, allowing the nanosheets in CoZnNi-OH to grow sufficiently. Furthermore, the element distribution of LDH samples was analyzed by EDS. As shown in Figs. 2d, h, l and Fig. S5 (Supporting information), all elements were uniformly distributed in the LDH samples.

The crystal structure of LDH samples were analyzed by X-ray diffraction (XRD). As shown in Fig. 3a, CoNi-OH, CoCuNi-OH, and CoZnNi-OH exhibit similar diffraction peaks belonging to the (003), (006), (012), and (110) crystal planes, which agree with the typical LDH structure (JCPDS No. 38–0715) [23]. The XRD peaks of the ZIF precursor almost disappear, indicating the successful phase conversion of ZIF to LDH. Importantly, the diffraction peak of the (003) crystal plane in CoCuNi-OH and CoZnNi-OH shifts, demonstrating the incorporation of Zn or Cu atoms in CoNi-OH makes the crystal unit parameter changes. The diffraction peaks of (003) crystal plane of CoNi-OH, CoCuNi-OH and CoZnNi-OH locate at 11.58°, 12.24° and 10.04°, respectively. According to the Bragg formula, the angle of the diffraction peak shifts left, indicating an increase in the interlayer spacing of the corresponding crystal plane [24,25]. The calculated interlayer spacing of CoNi-OH, CoCuNi-OH and CoZnNi-OH are 0.74, 0.72, and 0.88 nm, respectively. Therefore, the incorporation of Zn atom can increase the interlayer spacing of the (003) crystal plane in CoZnNi-OH (Fig. 3b and Fig. S6 in Supporting information). Fig. S7 (Supporting information) shows the Fourier transform infrared spectroscopy (FTIR) of the LDH samples. The absorption band near 3451 cm^{-1} belongs to the stretching vibration of O–H in the -OH group, and the band at 1631 cm^{-1} belongs to the bending vibration of H_2O molecules adsorbed between the LDH layers. The absorption band at 1320 cm^{-1} can be attributed to the symmetric stretching vibration of CO_3^{2-} between the LDH layers. Moreover, the absorption band appearing at 630 cm^{-1} belongs to the stretching vibration of M-O and M-OH. From the above analysis of XRD and FTIR, the phase of LDHs can be confirmed. Besides, the element composition and valence states of LDHs were analyzed. Fig. S8 (Supporting information) shows the full X-ray photoelectron spectroscopy (XPS) spectra of CoNi-OH, CoCuNi-OH, and CoZnNi-OH. Fig. 3c shows the O 1s high-resolution spectra of LDH samples, with peaks at 531.4 eV and 532.7 eV representing oxygen-containing functional groups bound to metal ions and hydroxyl bonds within adsorbed H_2O molecules, respectively. Fig. 3d is the Co 2p high-resolution XPS spectrum, with peaks at 783.1 eV and 798.1 eV corresponding to Co^{2+}, and peaks at 781.3 eV and 796.8 eV corresponding to Co^{3+}. The simultaneous presence of Co^{2+} and Co^{3+} indicates that Co^{2+} is partially

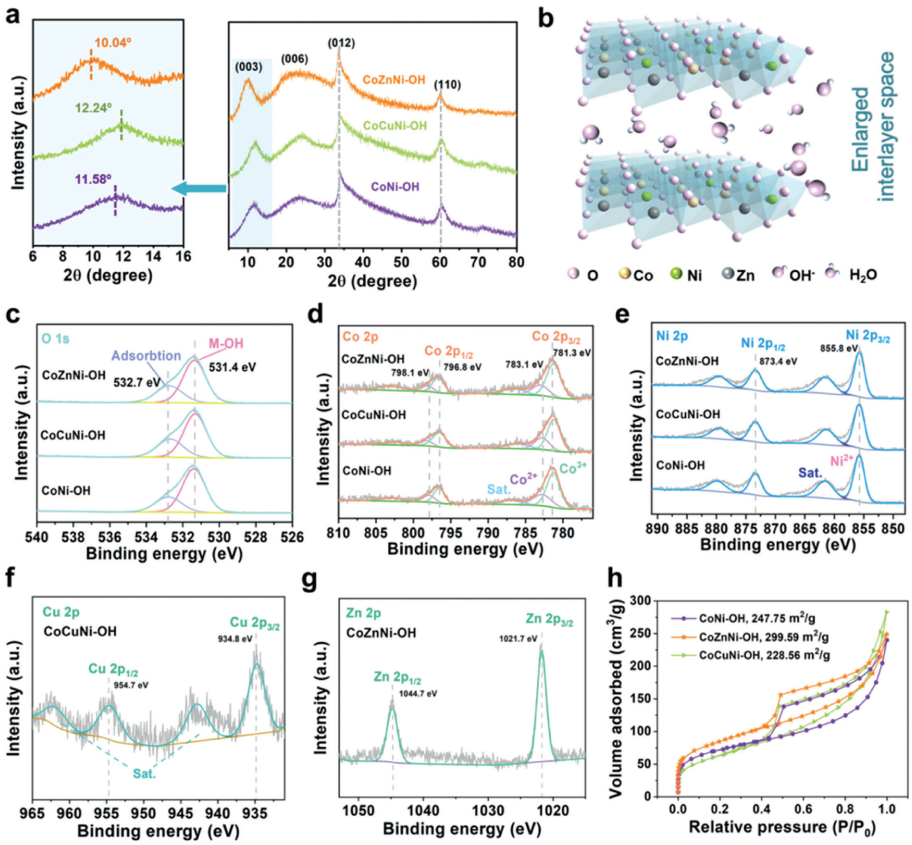

Fig. 3. (a) XRD of CoNi-OH, CoCuNi-OH, and CoZnNi-OH. (b) Crystal structure diagram of CoZnNi-OH. (c) O 1s, (d) Co 2p, (e) Ni 2p spectra of CoNi-OH, CoCuNi-OH, and CoZnNi-OH. (f) Cu 2p spectra of CoCuNi-OH. (g) Zn 2p spectra of CoZnNi-OH. (h) Nitrogen adsorption-desorption isotherms of CoNi-OH, CoCuNi-OH, and CoZnNi-OH.

oxidized by O_2 or NO_3^- dissolved in the solution during ion exchange reactions. Fig. 3e shows the XPS spectrum of Ni 2p, with peaks appearing at 855.8 eV and 873.4 eV representing Ni^{2+} with a spin separation energy of 17.6 eV, accompanied by vibrational satellite peaks at 861.5 eV and 879.6 eV. Fig. 3f show the valence of Cu in CoCuNi-OH, with peaks at 934.8 eV and 954.7 eV indicating the presence of Cu^{2+} [26]. Fig. 3g show the valence of Zn in CoZnNi-OH, with peaks at 1021.7 eV and 1044.7 eV corresponding to Zn^{2+} [27]. The specific surface of LDH samples is measure by N_2 adsorption/desorption. As Fig. 3h presented, CoNi-OH, CoCuNi-OH and CoZnNi-OH have similar N_2 adsorption/desorption curves, and CoZnNi-OH possesses the largest Brunauer-Emmett-Teller (BET) surface area of 299.59 m^2/g. Besides, Fig. S9 (Supporting information) depicts the pore size distribution plots of CoNi-OH, CoCuNi-OH and CoZnNi-OH, and the most Frequent pore diameter is around 2 nm.

The formation process of hollow LDH nanoboxes was deeply analyzed by varying the reaction time. The morphology of the samples collected at different reaction times is shown in Figs. 4a-j. As the reaction progresses to 5 min, the surface of pristine CoZn-ZIF becomes rough and the top corners become blunt. At 30 min, CoZn-ZIF was surrounded by LDH nanosheets, exhibiting a unique core-shell structure. At 120 min, the CoZn-ZIF core disappeared and the core-shell structure transformed into a hollow structure assembled from ultrathin nanosheets. At 240 min, the hollow structure collapsed significantly due to the excessive reaction. Based on the observed morphological changes, the formation process of LDH nanoboxes can be explained as follows. During the ion exchange process, Ni^{2+} slowly hydrolyzed in ethanol solvent and released protons, which effectively control the reaction process and prevent the structural collapse. Protons adsorbed on the surface of CoZn-ZIF while breaking the coordination bonds between metal ions and organic ligands. The released metal ions co-precipitate with Ni^{2+} on the surface of CoZn-ZIF, forming a CoZnNi-OH shell. As the reaction continues, the internal ZIF core becomes easily decomposed, ultimately forming a hollow LDH nanobox. Fig. 4k shows the XRD of samples with different reaction times. As the reaction goes, the characteristic peaks of the LDH phase increase. When the reaction reaches 30 min, both ZIF and LDH characteristic peaks appear in the samples. When the reaction reaches 120 min, only LDH characteristic peaks appear. As expected, the variation trend of XRD curves is consistent with the results observed in SEM and TEM images. In addition, similar trends were observed in the FTIR curves of the nanomaterials with different reaction times (Fig. 4l). To further understand the changes in metal content during the transformation processes, we used ICP-OES to test the metal contents of samples with different reaction times (Fig. 4m). During the reaction process, the Co element is constantly replaced by the Ni element, while the content of the Zn element changes very weakly. This phenomenon indicates that using bimetallic ZIF as precursors to prepare LDH can effectively regulate the ion content in the product.

The electrochemical performance of CoNi-OH, CoCuNi-OH, CoZnNi-OH (120 min), and CoZnNi-OH (240 min) electrodes were tested using a three-electrode system. Fig. 5a depicts the cyclic voltammetry (CV) of the electrodes at 5 mV/s and in a voltage window of 0–0.6 V. Each electrode has obvious oxidation and reduction peaks (Fig. S10 in Supporting information). The CoZnNi-OH (120 min) electrode exhibits the highest redox peak and the largest CV curve area, which implies can achieve the maximum specific capacity. Fig. 5b reveals the galvanostatic charge/discharge (GCD) curves of different electrodes at 10 mA/cm^2. As expected, the

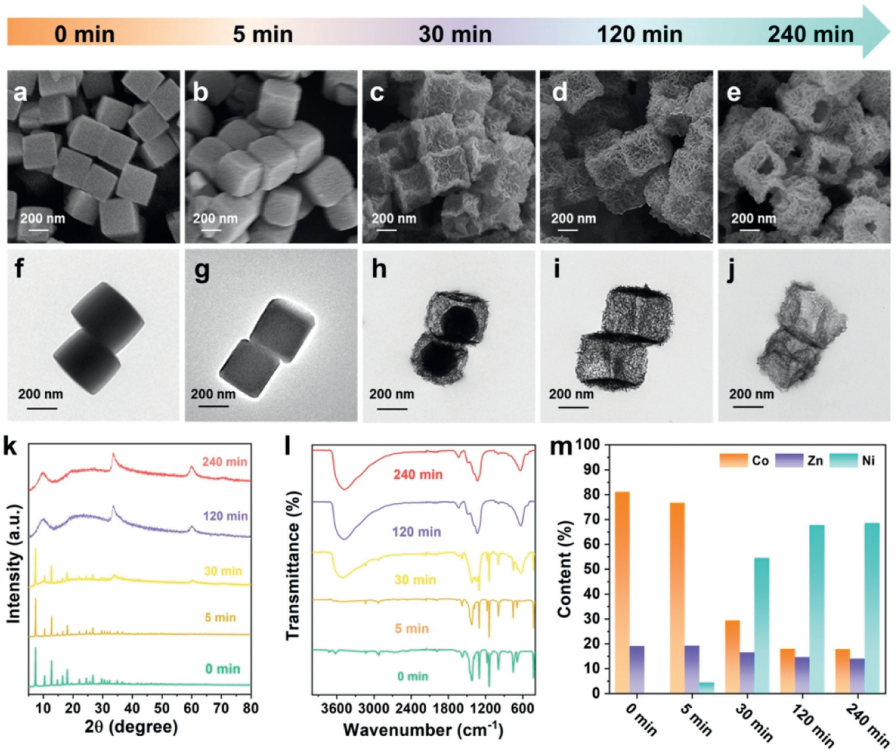

Fig. 4. SEM, and TEM images of (a, f) CoZn-ZIF (0 min), (b, g) CoZn-ZIF@CoZnNi-OH (5 min), (c, h) CoZn-ZIF@CoZnNi-OH (30 min), (d, i) CoZnNi-OH (120 min), (e, j) CoZnNi-OH (240 min). (k) XRD of different samples. (l) FTIR of different samples. (m) The content of metal elements in different samples.

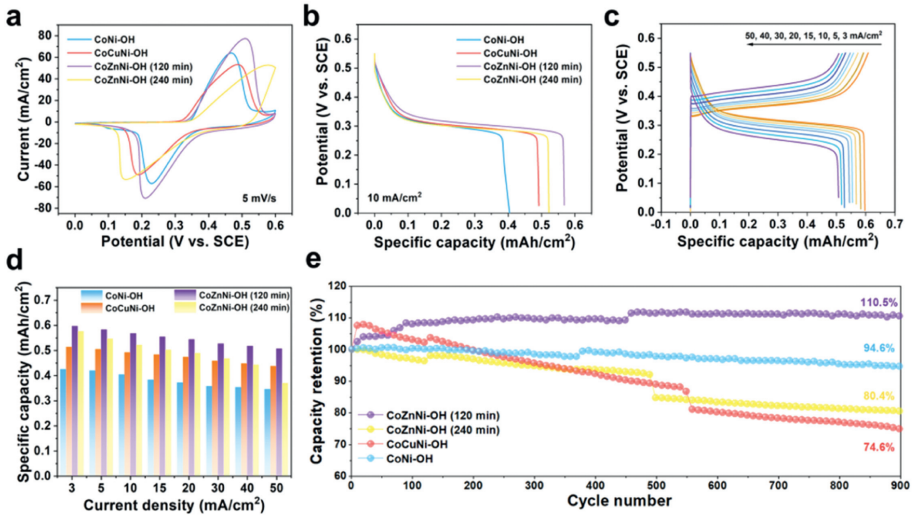

Fig. 5. (a) CV curves of different electrodes at 5 mV/s. (b) GCD curves of different electrodes at 10 mA/cm^2. (c) GCD curves of CoZnNi-OH (120 min) at different current densities. (d) Specific capacitance of different electrodes at diverse current densities. (e) Cycling stability of different electrodes.

CoZnNi-OH (120 min) electrode has the longest discharge plateau and the largest specific capacitance, which is consistent with the results reflected by CV curves (Fig. S11 in Supporting information). Furthermore, the GCDs of the CoZnNi-OH (120 min) electrode at various current densities is shown in Fig. 5c. When the current density is 3, 5, 10, 15, 20, 30, 40, and 50 mA/cm^2, the specific capacity of the CoZnNi-OH (120 min) electrode is 0.60, 0.58, 0.57, 0.56, 0.54, 0.53, 0.52, and 0.51 mAh/cm^2, respectively. The specific capacity of different electrodes at different current densities is summarized in Fig. 5d. The CoZnNi-OH (120 min) electrode reaches the maximum capacity retention of 85%. This can be attributed to the hierarchical hollow structure and relatively larger interlayer spacing of CoZnNi-OH (120 min), which provide large electrolyte contact surface area and promote rapid electron transfer and ion diffusion processes during electrochemical reactions [28]. Besides, the specific capacity of CoZnNi-OH (120 min), CoZnNi-OH (240 min), and CoCuNi-OH are generally higher than that of CoNi-OH. This is because the synergistic effect between multiple metallic elements is beneficial to expose more active sites for electrochemical redox reactions. Also, it is worth noting that the capacity of CoZnNi-OH (240 min) is close to that of CoZnNi-OH (120 min) at 1 mA/cm^2, while the capacity retention of CoZnNi-OH (240 min) at high current density is only 64%. This phenomenon can be attributed to the fact that CoZnNi-OH (240 min) has a similar com-

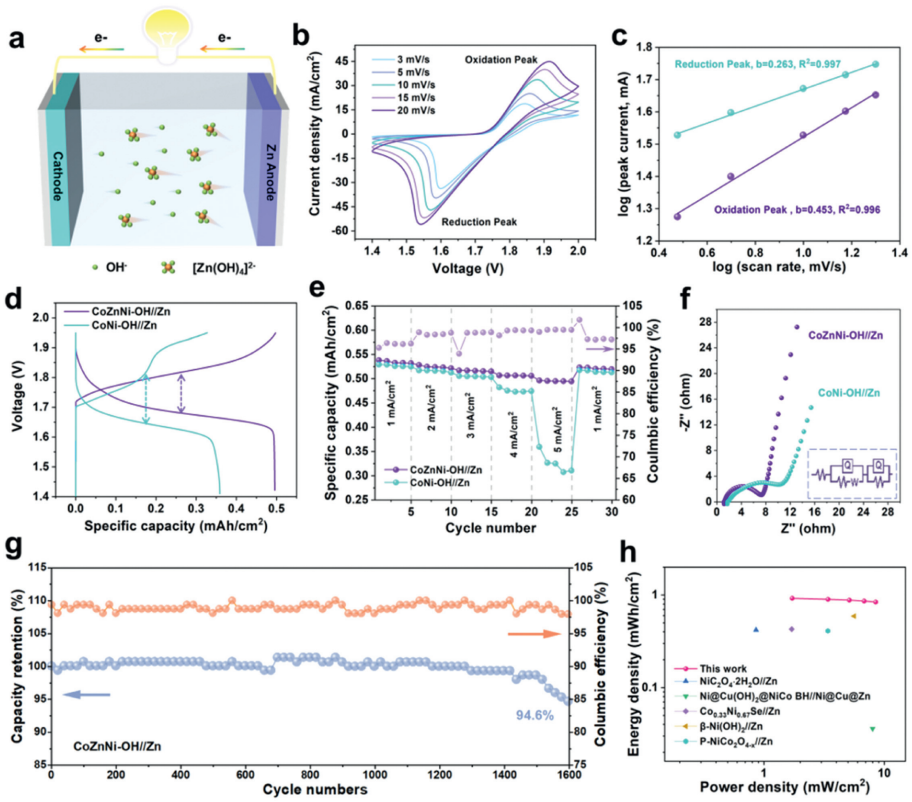

Fig. 6. (a) Mechanism diagram of aqueous zinc-based batteries. (b) CV curves of CoZnNi-OH//Zn at different scanning speeds. (c) log(i) *versus* log(v) plots of CoZnNi-OH//Zn. (d) GCD curves of CoZnNi-OH//Zn and CoNi-OH//Zn at 5 mA/cm^2. (e) The rate capability of CoZnNi-OH//Zn and CoNi-OH//Zn. (f) Nyquist plots of CoZnNi-OH//Zn and CoNi-OH//Zn (insert: equivalent circuit diagram). (g) Cycling stability of and coulomb efficiency of CoZnNi-OH//Zn. (h) Ragone diagram of CoZnNi-OH//Zn compared with other works.

position to CoZnNi-OH (120 min), but its structure collapses and the active sites reduced, resulting in poor electrochemical dynamics at high current densities. The cycling performance of different electrodes is presented at Fig. 5e. After 900 cycles of charge and discharge, the capacity of CoZnNi-OH (120 min) electrode is 110% of the initial capacity, while other electrodes show capacity decay. The outstanding cycling performance of CoZnNi-OH (120 min) further indicates that the integrated hierarchical hollow structure and the proper introduction of the Zn atoms can significantly enhance the stability of LDH.

To demonstrate the application possibility of CoZnNi-OH in alkaline aqueous zinc-based batteries, we assembled the CoZnNi-OH//Zn battery using CoZnNi-OH as the cathode and commercial zinc flake as the anode. Fig. 6a is a schematic diagram of the zinc-based batteries in alkaline aqueous systems. Fig. 6b reveals the CV curves of CoZnNi-OH//Zn at a high voltage window of 1.4–2.0 V. As the scan rate increases, the peak current gradually increases without significant deformation, implying the excellent reversibility of CoZnNi-OH//Zn. The energy storage mechanism is further measure by the formula $i = av^b$ (where a and b are constants, i represents the current and v represents the scan rate). According to the reduction/oxidation peaks of CoZnNi-OH//Zn, the b value is calculated as lower than 0.5, which demonstrate the battery is controlled by the diffusion process (Fig. 6c). Meanwhile, the CV curve and b value of the CoNi-OH//Zn battery is presented in Fig. S12 (Supporting information). Fig. S13 (Supporting information) presents the GCD curves of CoZnNi-OH//Zn and CoNi-OH//Zn. Fig. 6d further compares the GCD curves of CoZnNi-OH//Zn and CoNi-OH//Zn at 5 mA/cm^2. The charging/discharging plateau of CoZnNi-OH//Zn is 1.81/1.68 V, while the counterpart of CoNi-OH//Zn is 1.81/1.64 V [29]. Obviously, the CoZnNi-OH//Zn battery has a lower voltage hysteresis, indicating its lower polarization effect and better energy conversion efficiency. Fig. 6e shows the rate performance of CoZnNi-OH//Zn and CoNi-OH//Zn. When the current density is 1, 2, 3, 4, and 5 mA/cm^2, the average specific capacity of CoZnNi-OH//Zn is 0.54, 0.53, 0.52, 0.51, and 0.50 mAh/cm^2, respectively, and the counterpart of CoNi-OH//Zn is 0.53, 0.52, 0.51, 0.48, and 0.36 mAh/cm^2, respectively. Notably, the CoNi-OH//Zn presents poorer stability and repeatability at 5 mA/cm^2 than that of CoZnNi-OH//Zn. To support above phenomenon, we further tested the electrochemical impedance spectroscopy (EIS) of CoNi-OH//Zn and CoZnNi-OH//Zn to evaluate their electrochemical resistance. As shown in Fig. 6f, the CoZnNi OH//Zn has a smaller semicircle in the high-frequency region, indicating its smaller charge transfer resistance and faster ion and electron transfer rate. In addition, we test the long-term cycling stability of CoZnNi-OH//Zn (Fig. 6g and Fig. S14 in Supporting information). After 1600 cycles, the battery achieves high capacity retention of 94.6%. To further demonstrate the outstanding energy storage performance of CoZnNi-OH//Zn, we chart the Ragone diagram of CoZnNi-OH//Zn and other reported aqueous alkaline zinc-based batteries. As depicted in Fig. 6h, the maximum energy density/power density of our work is 0.924 mWh/cm^2, 8.479 mW/cm^2, which exceeds many other published zinc-based batteries (Table S1 in Supporting information) [30–34].

In summary, we designed bimetallic ZIF-derived LDHs with hierarchical hollow structure and adjustable interlayer spacing. The second metal (Zn or Cu) in bimetallic ZIFs can significantly affect the morphology of the derived LDH nanosheets that constitute the hollow assembly. Besides, the transformation mechanism of CoZn-ZIF into CoZnNi-OH proves the feasibility and controllability for obtaining well-defined LDHs. Importantly, the hierarchi-

cal hollow architecture and enlarger interlayer spacing of CoZnNi-OH optimized the overall electrochemical activity including electrolyte infiltration efficiency, charge transfer rate, and redox reaction dynamitic. Especially for the aqueous alkaline CoZnNi-OH//Zn battery, the maximum energy density/power density reached 0.924 mWh/cm^2, 8.479 mW/cm^2. This work provides a valuable reference to co-engineering the hollow architecture and interlayer spacing of LDH for aqueous batteries.

Declaration of competing interest

The authors declare that they have no known competing financial interests or personal relationships that could have appeared to influence the work reported in this paper.

CRediT authorship contribution statement

Hui Yang: Writing – original draft. **Guangxun Zhang:** Investigation. **Yueyao Sun:** Investigation. **Huijie Zhou:** Investigation. **Huan Pang:** Conceptualization.

Acknowledgments

This work was supported by the National Natural Science Foundation of China (Nos. 52371240, U1904215), Natural Science Foundation of Jiangsu Province (No. BK20200044), Changjiang scholars' program of the Ministry of Education (No. Q2018270).

Supplementary materials

Supplementary material associated with this article can be found, in the online version, at doi:10.1016/j.cclet.2024.110016.

References

[1] Z. Yu, N. Ji, X. Li, et al., Angew. Chem. Int. Ed. 62 (2023) e202213612.
[2] J. Xiao, K. Cheng, X. Xie, et al., Nat. Mater. 21 (2022) 572–579.
[3] Z.L. Zheng, M.M. Wu, X. Zeng, et al., Angew. Chem. Int. Ed. 63 (2024) e202400012.
[4] Y. Tang, J. Ding, W. Zhou, et al., Adv. Sci. 10 (2023) 2206960.
[5] L. Guo, Z. Mu, P. Da, et al., Energy Chem 4 (2022) 100088.
[6] W. Bai, R. Wu, Z. Xue, et al., Adv. Funct. Mater. 34 (2024) 2401421.
[7] H. Zhang, S. Zhang, B. Guo, et al., Angew. Chem. Int. Ed. 63 (2024) e202400285.
[8] D. Zhao, Y. Wei, J. Xiong, C. Gao, D. Wang, Adv. Funct. Mater. 33 (2023) 2300681.
[9] Z. Ji, G. Tang, L. Chen, et al., Chem. Eng. J. 480 (2024) 148213.
[10] S. Zheng, Y. Sun, H. Xue, et al., Natl. Sci. Rev. 9 (2022) nwab197.
[11] G. Zhang, Y. Li, X. Xiao, et al., Nano Lett. 21 (2021) 3016–3025.
[12] X. Li, J. Liu, K. Zhou, et al., J. Am. Chem. Soc. 144 (2022) 21702–21709.
[13] S. Wang, L. Luo, A. Wu, et al., Coord. Chem. Rev. 498 (2024) 215464.
[14] C. Zhang, L. Yuan, C. Liu, et al., J. Am. Chem. Soc. 145 (2023) 7791–7799.
[15] Z. Qiu, Y. Li, Y. Gao, et al., Angew. Chem. Int. Ed. 62 (2023) e202306881.
[16] J. Ma, J. Xia, Z. Liang, et al., Small 17 (2021) 2104423.
[17] J. Li, Y. Xie, M. Cao, Y. Feng, J. Yao, J. Colloid Interface Sci. 631 (2023) 222–230.
[18] X. Zhang, P. Xing, T.L. Madanu, et al., Natl. Sci. Rev. 10 (2023) nwad235.
[19] P. Ruan, S. Liang, B. Lu, H.J. Fan, J. Zhou, Angew. Chem. Int. Ed. 61 (2022) e202200598.
[20] L. Li, Q. Cao, Y. Wu, et al., Adv. Mater. 35 (2023) 2300132.
[21] G. Li, Y. Tang, S. Cui, et al., Adv. Funct. Mater. 34 (2024) 2401586.
[22] G. Zhang, H. Yang, H. Zhou, et al., Angew. Chem. Int. Ed. 63 (2024) 202401903.
[23] W. Qiu, G. Li, D. Luo, et al., Adv. Sci. 8 (2021) 2003400.
[24] L. Peng, N. Yang, Y. Yang, et al., Angew. Chem. Int. Ed. 60 (2021) 24612–24619.
[25] Q. Pan, F. Zheng, D. Deng, B. Chen, Y. Wang, ACS Appl. Mater. Interfaces 13 (2021) 56692–56703.
[26] D. Sengupta, P. Melix, S. Bose, et al., J. Am. Chem. Soc. 145 (2023) 20492–20502.
[27] Y. Kong, Y. Li, X. Sang, et al., Adv. Mater. 34 (2022) 2103548.
[28] T. Chen, L. Xue, Z. Shi, et al., ACS Appl. Mater. Interfaces 14 (2022) 54369–54388.
[29] Y. Su, J. Hu, G. Yuan, et al., Adv. Mater. 35 (2023) 2307003.
[30] T. Chen, Y. Bai, X. Xiao, H. Pang, Chem. Eng. J. 413 (2021) 127523.
[31] D. Zhang, B. Jiang, Y. Liu, et al., New. J. Chem. 46 (2022) 14451–14457.
[32] T. Chen, Z. Shuang, J. Hu, et al., Small 18 (2022) 2201628.
[33] Y. Zeng, Z. Lai, Y. Han, et al., Adv. Mater. 30 (2018) 1802396.
[34] F. Sun, T. Chen, Q. Li, H. Pang, J. Colloid Interface Sci. 627 (2022) 483–491.